Journal of Power Sources 192 (2009) 475–485

Contents lists available at ScienceDirect

Journal of Power Sources

journal homepage: www.elsevier.com/locate/jpowsour

Experimental study of clamping effects on the performances of a single proton exchange membrane fuel cell and a 10-cell stack

Chih-Yung Wen*, Yu-Sheng Lin, Chien-Heng Lu

Department of Aeronautics and Astronautics, National Cheng-Kung University, No.1, Ta-Shieh Rd., Tainan 70101, Taiwan

ARTICLE INFO

Article history:
Received 20 January 2009
Received in revised form 9 March 2009
Accepted 11 March 2009
Available online 5 April 2009

Keywords:
Proton exchange membrane fuel cell
Mean contact pressure
Non-dimensional pressure fluctuation intensity

ABSTRACT

The contact pressure distribution is known to have significant influences on the contact ohmic resistance, porosity of gas diffusion layers (GDLs) and performance of the proton exchange membrane fuel cell (PEMFC) consequently. This work experimentally investigated the effects of various combinations of bolt configuration and clamping torque on the corresponding contact pressure distributions and performances of a single PEMFC and a 10-cell stack. The pressure-sensitive films (FUJI-FILM I&I) were used to visualize the contact pressure distributions under three different clamping torques and three different bolt configurations in the experiments. The importance of the proper stacking design was clearly demonstrated by these contact pressure images. The mean value and the fluctuation intensity of the contact pressure were extracted statistically from the data of pressure-sensitive films. A non-dimensional pressure fluctuation intensity, which indicates the relative dispersion to its mean value, was proposed to gauge the uniformity of the contact pressure distribution, similar to the definition of the turbulence intensity in fluid mechanics. The experimental results showed that, for the single cell under the current experiment conditions, the larger mean contact pressure tends to yield the higher maximum power, regardless of the bolt configuration and the applied torque. The uniformity of the contact pressure distribution, the ohmic resistance and the mass transport limit current had highly linear correlations with the mean contact pressure. In the case of the 10-cell stack, the effects of various combinations of bolt configuration and clamping torque on its performance and the mass transport limit current could not be reflected by the stack mean contact pressure only. Increasing the mean contact pressure improved the uniformity of the contact pressure distribution and reduced the contact ohmic resistance, in general. However, the maximum power did not increase monotonically with the mean contact pressure and no linear correlation was found. The detailed contact pressure distribution may have important influences on the local electrochemical reactions and heat and mass transfer processes involved in the stack.

1. Introduction

Polymer electrolyte membrane fuel cell (PEMFC) is an electrochemical device that directly converts the chemical energy of reaction gases, for example, hydrogen and oxygen or air, into electricity, without generating pollutions. Thus, countries worldwide pay more attention to the development of this so-called "clean" energy generation technology and drive it to be one of the alternative energy sources in the future. The operation temperature of a PEMFC is relatively low (60–100 °C) and offers a short start-up and shut down time (few minutes).

A PEMFC suffers the voltage losses which affect its performance and are primarily caused by three sources: activation polarization, ohmic polarization and concentration polarization [1]. The activation polarization loss is due to the simultaneous occurrence of the two-electron and four-electron oxygen reduction reactions. Ohmic losses vary directly with current, increasing over the entire range of current density. Ohmic losses can be improved by using different assembly mechanisms and forces, membrane electrode assembly (MEA) and bipolar plate materials and designs of the flow channel plates to lower the carrier-conducting resistance and the electric contact resistances at various interfaces. The concentration polarization losses occur due to the mass transport limitation of reactants/products to or from the electro-active sites. Mass transport voltage losses occur over the entire range of current density, but become prominent especially at high limiting currents, when it is difficult to provide enough reactant flows to the reaction sites. The mass transport voltage losses can be reduced by making the gas distribution over the electrode surfaces more uniform with proper designs of the flow channel and assembly mechanism, and by using the backing layers with higher porosity (interconnected pores).

* Corresponding author. Tel.: +886 6 2757575x63657; fax: +886 6 2349281.
E-mail address: cywen@mail.ncku.edu.tw (C.-Y. Wen).

0378-7753/$ – see front matter © 2009 Elsevier B.V. All rights reserved.
doi:10.1016/j.jpowsour.2009.03.058

Nomenclature

b	Tafel slope (Eq. (1), mV per decade)
E	measured cell voltage (V)
E_r	reversible potential for the cell (Eq. (4), V)
I, i	measured cell current density ($A\,m^{-2}$)
i_d	mass transfer parameters at high current range (Eqs. (1)–(3), A)
i_m	mass transfer parameters at high current range (Eqs. (1)–(3), A)
i_0	exchange current density (Eq. (4), $A\,m^{-2}$)
M	total number of cells in a stack
m	mass transfer parameters at high current range (Eq. (1), Ω)
N	total number of pixels in a scanned pressure-sensitive film image
n	mass transfer parameters at high current range (Eq. (1), A^{-1})
$P(P_{ij})$	pressure (at pixel (i,j)) (MPa)
$\bar{P}(\overline{P_j})$	cell mean contact pressure (of cell no. j) ($\equiv (\sum P_{ij})/N$, MPa)
$\overline{\overline{P_j}}$	mean pressure value of a stack ($\overline{\overline{P_j}} \equiv (\sum \bar{P}_j)/M$, MPa)
$P'(P'_j)$	standard deviation of the cell pressure distribution (of cell no. j) $\left(\equiv \sqrt{(1/(N-1))\sum (P_{ij}-\bar{P})^2},\ \mathrm{N\,m^{-2}}\right)$
$P'/\bar{P}$	non-dimensional pressure fluctuation intensity of a single cell
$\overline{(P'/\bar{P})_j}$	mean non-dimensional pressure fluctuation intensity of a stack ($\equiv (\sum (P'/\bar{P})_j)/M$)
R	ohmic resistance of a single cell ($\Omega\,cm^2$)
W_{max}	maximum power (W)

Greek symbols

σ_z	compression stress ($N\,m^{-2}$)
τ	clamping torque (N m)

Fig. 1 shows the components and clamping sequence of a PEMFC stack, including end plates, insulating plates, collector plates, MEAs and bipolar plates. In general, the fuel cell clamping can be categorized into three types: point-load design, line-load design and surface-load design [2]. The traditional and most popular point-load design with the assembly of several pairs of bolts and nuts is adopted in this study. Because clamping configuration of the point-load design will affect the contact behavior between bipolar plates and MEAs, the clamping torque and bolt configuration (number of bolts and their positions) are considered as the important factors that determine the uniformity of contact pressure on the MEAs and hence affect the performance of the PEMFC system. The proper-designed clamping configuration will prevent leaking, homogenize the contact pressure distribution within the fuel cell stack and minimize the interfacial electric contact resistance. Uneven distribution of the contact pressure may cause hot spots which will have a detrimental effect on fuel cell life.

Lee et al. [3] experimentally investigated the effects of changing the clamping torque and gas diffusion layer (GDL) on the performance of a PEMFC at fixed 4-bolt configuration and stoichiometric flow rates for the fuel and reactant. For the three torques used in their experiments, an optimal bolt torque in terms of power density was obtained for each GDL. This optimum was explained in terms of the changes in the porosity and the electrical contact resistance. A higher clamping force gives a lower interfacial electric contact resistance, but also gets a lower GDL porosity. The electric contact resistance decreases rapidly with the initial increase in the clamping force and then remains virtually unchanged after reaching relatively large compression force. Hence, for the case of a more compressible GDL material, the cell performance increased with the clamping torque until an optimal clamping torque was reached. Further increase of the clamping torque resulted in the performance deterioration because of the continuous decrease of the GDL porosity. For the case of a less compressible and somewhat brittle material, the results showed that higher performance was obtained with less torque indicating that the higher bolt torque may have damaged the GDL. Mishra et al. [4] measured the electrical contact resistance between flow channel plate and GDL. The measured contact resistance values were compared with predictions of contact resistance model based on a fractal representation of the interface geometry. Good agreement is observed between the data and the model predictions for a wide range of contact pressures and materials. In order to achieve a uniform contact pressure distribution, Wang et al. [5] designed and fabricated a pressurized end plate with a built-in hydraulically pressurized pocket covered by a thin wall facing the fuel cell assembly. Pressure-sensitive films were used to measure the pressure distribution for both conventional point-load bolt-fastening and their newly designed surface-load hydraulic mechanisms. It was found that the contact pressure distribution for the hydraulic compression mechanism was more uniform than for the conventional bolt-fastening design. Consequently, an improved fuel cell performance was shown for the newly designed clamping system. Many other stacking designs have also been proposed to achieve a uniform contact pressure distribution [6–8].

Other than experimental investigations, finite element analysis (FEA) models were used to analyze the contact pressure distribution. Lee et al. [9] established FEA procedures for a PEM single cell with point-load assembly design. The results of the analysis were compared with the actual contact pressure distributions measured by pressure-sensitive films. The trends of the simulated and measured pressure distributions were similar. Zhou et al. [10] built a simplified two-dimensional FEM analysis model of a PEM single cell with interdigitated gas distributors to analyze the elastic deformation of the GDL and the interfacial contact pressure. Then, the porosity distribution, the changed volume in the flow channels and the interfacial electric contact resistance were calculated and inputted into a finite volume flow solver to investigate the effect of clamping force on the mass transport of the reactants and products and the performance of the PEMFC. It is shown that the clamping force affects the permeability and diffusion of the reactant gas and the transport of the liquid water due to the GDL deformation and the porosity.

An inadequate clamping force increases the interfacial electrical resistance, but an excessive clamping force decreases the GDL porosity and thus increases the transport resistance of the gas and liquid water. There would be a maximum power density if an optimal clamping force is found for a practical fuel cell system. Liu et al. [11] performed a robust design analysis based on response surface methodology on a simplified two-cell stack model to identify the effect of the assembly parameters on the MEA pressure distribution. A FEM model of four bolt and nut assemblies was built to obtain the membrane's maximum and minimum compression stress $\max \sigma_z$ and $\min \sigma_z$. The assembly pressure and bolt position were considered as randomly varying design variables with given probabilistic property. $\mathrm{Max}\,\sigma_z$ and the $\Delta\sigma_z$ ($\equiv \max \sigma_z - \min \sigma_z$) were used for the desirability function of the optimal design. $\mathrm{Max}\,\sigma_z$ represents the value of contact pressure and $\Delta\sigma_z$ represents the uniformity of MEA pressure distribution. When $\max \sigma_z$ increases, it means the contact pressure on MEA becomes larger. If $\Delta\sigma_z$ decreases, the uniformity of MEA pressure distribution will become better. The reliability of the robust design has been demonstrated.

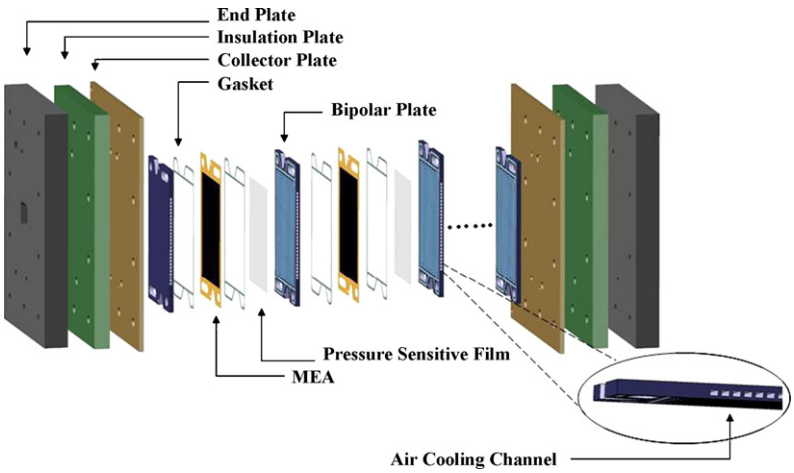

Fig. 1. Schematic of the PEMFC stack.

As shown, the most important goal in the assembly design is to achieve a proper and uniform contact pressure distribution. Nevertheless, the general criteria for the "uniform distribution" have not been rigorously defined in the literature. In this study, it is aimed to investigate experimentally the effects of the assembly pressure and the bolt configuration (number of bolts and their positions) on the performance of a PEMFC and a 10-cell stack at fixed stoichiometric flow rates for the fuel and reactant. In order to find the relationship between the assembly variables (assembly pressure and bolt configuration) and the performance of the PEMFC, statistical analysis was performed on the contact pressure distribution obtained from the pressure-sensitive film. A non-dimensional pressure fluctuation intensity was found to represent the uniformity of contact pressure distribution.

2. Experimental

2.1. Design and assembly of a single PEM fuel cell and a 10-cell stack

Fig. 1 schematically depicts the fuel cell stack used in our research. The fuel cell stack had 10 single cells assembled in series. Brief details about each component are described in this section. Pelcan® graphite bipolar plates of dimension 155 mm × 85 mm × 4 mm with three-parallel-channel serpentine flow fields for both cathode and anode were used. The channel width and height were 1 and 0.6 mm, respectively. Parallel straight air cooling channels were placed in the middle of every bipolar plate. Each cooling channel has a rectangular cross-section of 3 mm × 2 mm. Two fans were placed on top of the stack to provide necessary cooling. Both sides of MEA were sealed with green silicon rubber sealing-rings of 0.8 mm diameter placed inside the O-ring grooves on the peripheries of bipolar plates to ensure gas tight sealing. The O-ring groove is 0.8 mm wide and 0.3 mm deep. Therefore, the O-rings will be 0.5 mm higher than the surfaces of the bipolar plates. The MEA (a Nafion® 112 membrane with catalyst loading of anode and cathode: Pt/Ru 0.5 mg cm^{-2} and Pt 0.65 mg cm^{-2}) sandwiched in between two standard TORAY® carbon papers (TGP-H-090) as GDLs were placed in the middle of two flow channel plates. The active area of each MEA was 100 cm^2. End plates were aluminum alloy (6061T651) with dimensions of 250 mm × 180 mm × 20 mm. POM insulation plates and copper current collectors were placed between the end plate and stack. For the case of the single cell, only one cell was placed between the end plates and no fan was used in the experiment.

Bolts and nuts were used to tighten the PEM single cell and the stack. Fig. 2 shows the position of bolts on the end plates for configurations with 2, 4 and 6 bolts. During the stack assembly, two positioning rods were used for the alignment. The end plate, insulation plate, current collector, bipolar plate, MEA, etc. were aligned and stacked one by one. The sizes of SS 304 bolts are M10 × 1.25 mm with the length 107 mm for the single cell and 157 mm for the stack. Equal torque was applied on each bolt to assemble the PEM single cell and stack.

2.2. The contact pressure measurement methods

Before conducting the fuel cell performance tests, an experimental study was planned to measure the internal contact pressure distribution for different bolt torque and configuration. As shown in Fig. 1, pressure-sensitive films of thickness 90 ± 5 μm (Fuji 'Ultra Super Low' [12]) were used to reveal the contact pressure during these off-line experiments. The detective range of the chosen pressure-sensitive film is 0.2–0.6 MPa. Each piece of film was cut with the dimensions of 8.5 cm × 11.5 cm and was inserted on cathode side between the active area of MEA and bipolar plate. A torque spanner was used to lock and assemble the stack components. Note that these films were removed during on-line operation. Pressure-sensitive films have been used in the Refs. [3,5,9] to measure the internal contact pressure distributions for different assembly methods of fuel cells. Due to the small thickness of the pressure-sensitive film comparing with the allowable compression of O-ring (0.5 mm in the current experiments), the effect of the thickness of pressure-sensitive film on the internal contact pressure distribution was assumed negligible, as was done in Refs. [3,5,9].

The single cell and the 10-cell stack of the three different bolt configurations were assembled with torques τ of 8, 12 and 16 N m in a certain sequence as shown in Fig. 2. In our another study based on finite element analyses with the same configuration and component material properties of the PEM fuel cell [13], the maximum clamping torque was found close to 16 N m. At this clamping torque and 6-bolt configuration, the maximum stress in the PEM was found to be 5.8 MPa in the simulation, which is very close to the yielding strength of 6.14 MPa for the thin Nafion® 112 membrane obtained in a simple tension test by Tang et al. [14]. Further increase of the clamping torque may possibly cause the damage to PEMs. Due to a large number of PEMs needed in the experiments, especially in the stack experiments, which are very costly for researchers, the clamping torque was limited to 16 N m in this study.

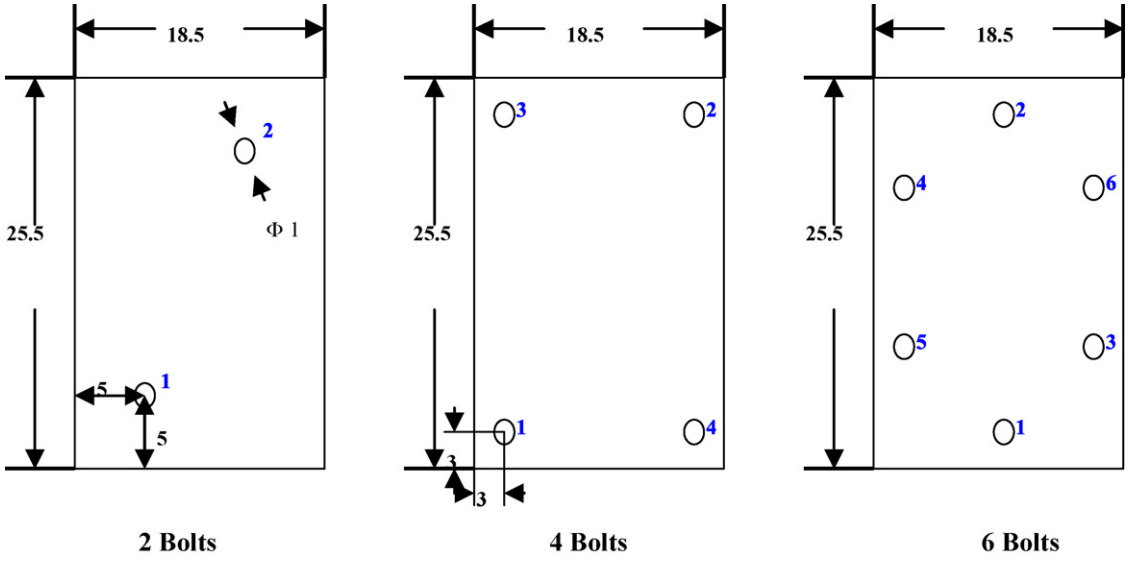

Fig. 2. Schematic drawing of the bolts' configuration (number of bolts and their positions). Numbers in blue represent the clamping sequence. (For interpretation of the references to color in this figure legend, the reader is referred to the web version of the article.)

Incremental torque settings of quarter-circle increments were applied until the final torque was reached. This procedure of the application of torque was followed according to the suggestion of United State Fuel Cell Council (USFCC) [15] to improve the reproducibility of the clamping behaviors. When the torque was applied, microcapsules on the pressure-sensitive film were broken and a color-forming material was released and absorbed on the film. The color (red) intensity of the film increases with the amount of applied pressure. At 5 min after it was assembled, the fuel cell unit was opened, and the pressure distribution on each film was observable by the color density pattern formed. Because the pressure values in the flow channel region are very small, compared with that under the ribs, a mask of the profile as that of the flow channels was applied on every color transformed pressure film. The filtered pressure film was then transferred into an image file by scanning. A Matlab program was written to transfer the color image file into a gray level bitmap file which was then compared with the reference color bar to obtain the pressure value [16]. The mean value $\bar{P}(\equiv(\sum P_{ij})/N)$ and the standard deviation $P'\left(\equiv\sqrt{(1/(N-1))\sum(P_{ij}-\bar{P})^2}\right)$ of the filtered pressure distribution were calculated afterward, where P_{ij} is the pressure at pixel (i, j) and N is the total number of pixels. Note that the pressure data in the flow channel region will form a low peak in the pressure distribution if not filtered out.

Following the incremental torque settings of USFCC [15], every single-cell case at given bolt configuration and clamping torque was repeated five times. The measured contact pressure contours from the pressure-sensitive films for each case were very similar and the mean value $\bar{P}$ and the standard deviation P' of the filtered pressure distribution were reproducible to within 0.025 $\bar{P}$ and 0.018 P', respectively.

2.3. I–V curve measurements

The *I–V* curves were measured on a computer-controlled Arbin fuel cell test system (Arbin Instruments, BT2000, 1 kW) which composed of an electrical load and a gas handling system to control the load and anode and cathode gas parameters such as flow rate, dew point temperature. The experimental setup has been described in detail in our previous work [17]. Pure hydrogen from the gas bottle and air from the oil-free compressor were regulated by flow controllers inside the gas handling system before fed into the cell. Both hydrogen and air pressure regulators at the test station were set at 3 bar G. The electrodes were purged with nitrogen between two measurements to realize reproducible initial conditions. The PEM single cell or stack was connected to the electrical load that was operated in a constant voltage discharge mode. The current and voltage of the fuel cell unit under operation, gas flow parameters like volume flow rates, relative humidity and temperatures of air and hydrogen were recorded with the data acquisition system.

The stack electrical insulation and gas leakage tests follow the procedures of Giddey et al. [18]. The stack was tested for electrical short-circuiting by measuring voltage between different components of the stack, i.e. between individual bipolar plates, between current collector plates (positive and negative), between current collector plates and the first and last bipolar plates, or between current collector plates and stack end plates. Nitrogen gas was used to test the gas leakage from hydrogen and air compartments, and cross-leakage from one compartment to the other.

2.4. Experimental conditions

The experimental results presented in the next section have been gained under the following conditions:

- Every MEA underwent an activation process suggested by USFCC [15] to ensure that fuel cell has reached a stable status for every test. The process involved running the PEM single fuel cell and the stack at:(1) 0.6 V for 60 min; (2) 0.7 V for 20 min; (3) 0.5 V for 20 min; (4) repeat steps (2) and (3) for nine times; (5) 0.7 V for 20 min; (6) open-circuit potential for 1 min.
- In the single cell performance test, the hydrogen gas was humidified to 80% RH at 65 °C with the flow rate of 300 sccm. Air was humidified to 80% RH at 65 °C with the flow rate of 1.5 slpm.
- In the 10-cell stack performance test, the hydrogen gas was humidified to 80% RH at 65 °C with the flow rate of 3 slpm. Air was humidified to 80% RH at 65 °C with the flow rate of 15 slpm.
- The atmospheric temperature was 25 °C.

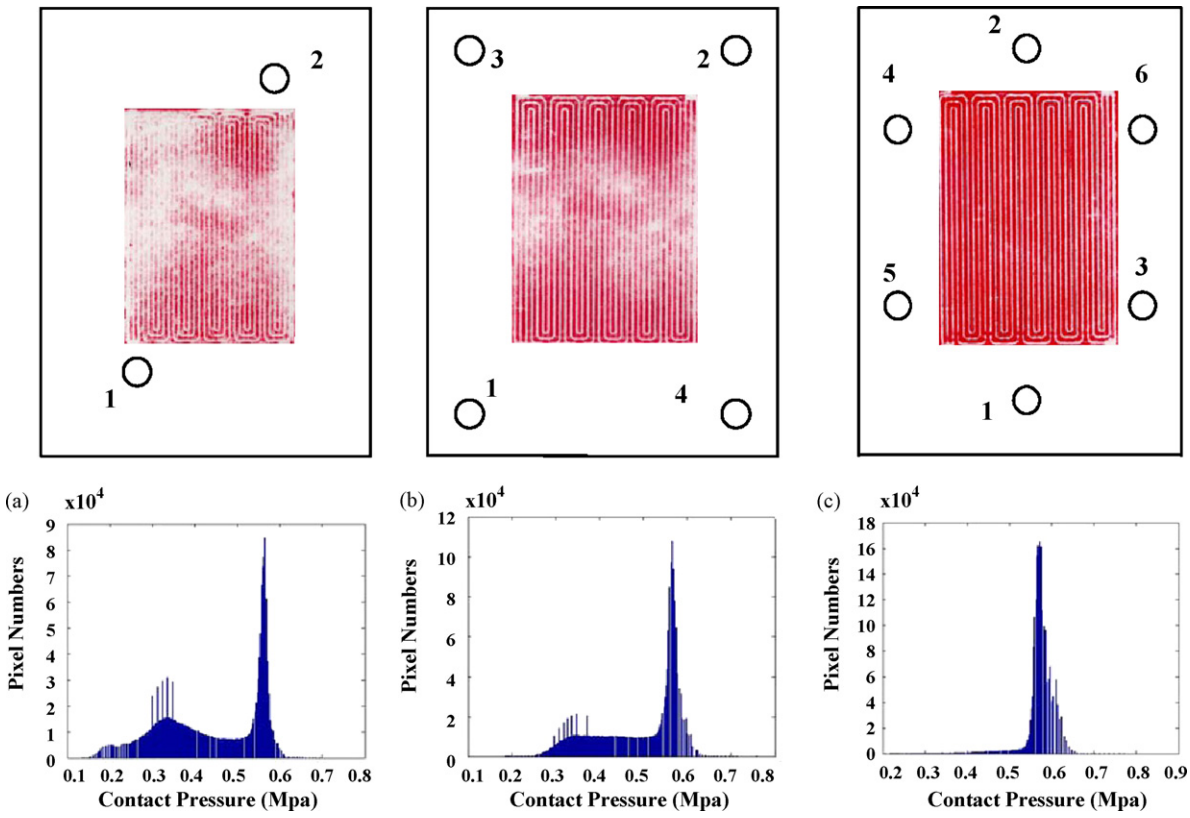

Fig. 3. Measured contact pressure contours from the pressure-sensitive films (top) and the corresponding statistic distributions (bottom) at (a) 2-, (b) 4- and (c) 6-bolt configurations and 16 N m clamping torque for each pair of bolt and nut in the case of a single cell. Outer frames and numbers in the top figures represent the boundaries of the end plates and the clamping sequence, respectively.

3. Results and discussion

3.1. Results of single cell

Fig. 3(a–c) shows the measured contact pressure contours from the pressure-sensitive films and the corresponding statistic distributions at 16 N m clamping torque (for each pair of bolt and nut) and 2-, 4- and 6-bolt configurations, respectively, in the single cell. In the upper images of Fig. 3(a–c), the color (red) intensity of the film indicates the level of applied pressure. The lighter the image, the less the contact pressure level. The imprint mark of the flow channel in Fig. 3(a) is light and sparse meaning that the pressure level is low and not uniform in general. This assembly configuration is in-effective and not recommended for uniform contact pressure distribution. The level and uniformity of contact pressure distribution increase as pairs of bolt and nut increase, at the same clamping torque. As shown in Fig. 3(c), the imprint mark of the flow channel is clear and uniform for the case of 6-bolt configuration. Note that the color intensity at the upper right and lower left corners in Fig. 3(a), and at four corners in Fig. 3(b) is darker than the rest of regions. The bending of the end plates yields the lighter color images in the middle of the contact pressure contour in Fig. 3(b). These contact pressure distributions correlate well with the bolt locations and clearly demonstrate the importance of the proper stacking design. The measured distributions were non-symmetric due to the assembling sequence and other actual physical imperfection including minor positioning errors, flatness error of the bipolar plates ..., etc.

The contact pressure distributions obtained from the statistic analyses of the scanned bitmap images of the pressure-sensitive films are shown in the bottom half of Fig. 3. As seen, the more pairs of bolt and nut, the narrower the contact pressure distribution. In Fig. 3(a), a double-peak and wide distribution is observed for the 2-bolt configuration. On the other hand, a nearly normal and concentrated distribution is seen in Fig. 3(c) for the 6-bolt case. The statistic distributions are in good agreement with that of the imprint images.

At a fixed bolt configuration, the effects of increasing the clamping torques are exemplified in Fig. 4(a–c). The measured contact pressure contours and the corresponding statistic distributions at 4-bolt configuration show higher pressure amplitudes and more uniform pressure distribution at larger clamping torques. Again, in all three cases, the color intensity at four corners in is darker than the rest of regions due to the bending of the end plates.

The mean value and the standard deviation of the pressure distribution of every combination of bolt configuration and applied torque in the case of a single cell were calculated and presented in Table 1. The mean value $\bar{P}$ and the standard deviation P' are measures of the magnitude and dispersion of the contact pressures. As expected, $\bar{P}$ increases with the clamping torque τ at a given bolt configuration, and increases with the bolt numbers at a fixed τ. However, P' does not show any similar or opposite trend to that of $\bar{P}$. A non-dimensional pressure fluctuation intensity $P'/\bar{P}$, which indicates the relative dispersion to its mean value, was proposed to present the uniformity of the contact pressure distribution, similar to the definition of the turbulence intensity in fluid mechanics. As seen in Table 1, an opposite trend as that of $\bar{P}$ is obtained. $P'/\bar{P}$ decreases with the increase of the clamping torque τ at a given bolt configuration, and decreases with the increase of the bolt numbers at a fixed τ.

The polarization and power density curves describing the performances of the single cell at 2-, 4- and 6-bolt configurations are presented in Fig. 5(a–c), respectively. The maximum power density increases and the mass transport limitation shifts to higher

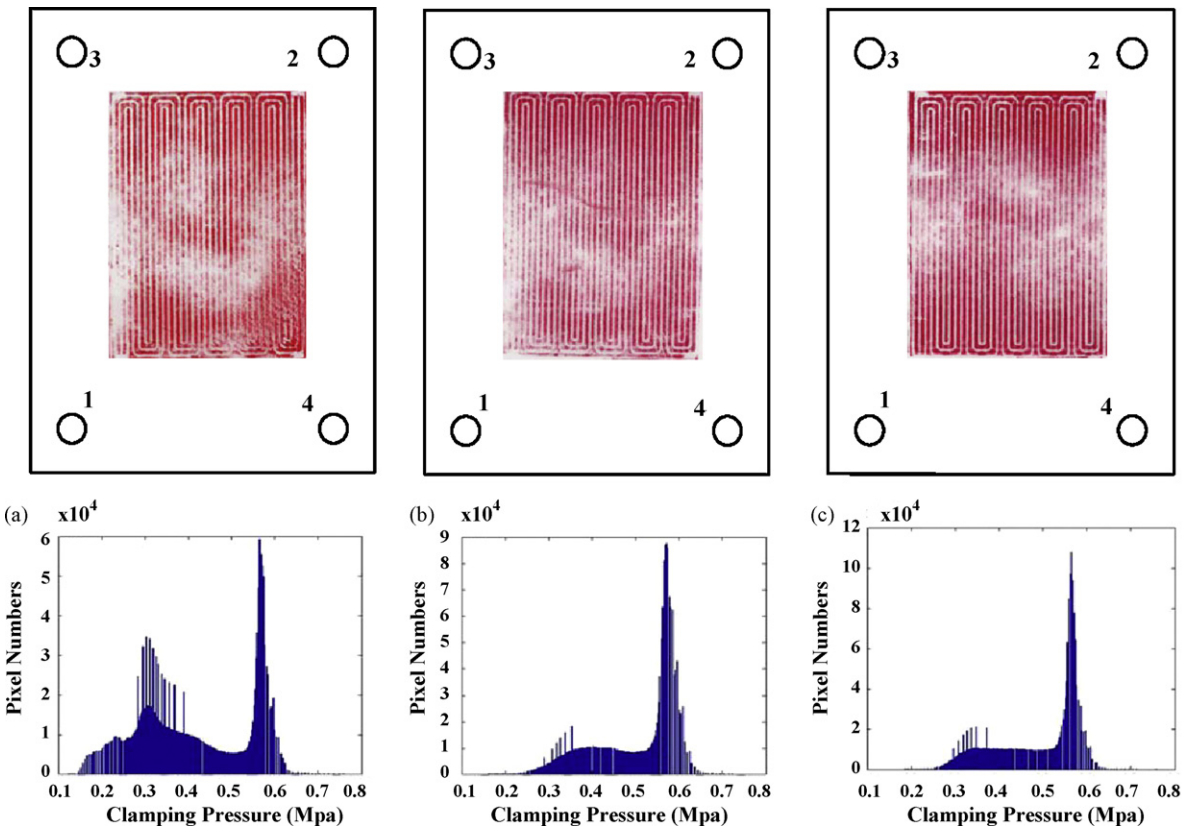

Fig. 4. Measured contact pressure contours from the pressure-sensitive films (top) and the corresponding statistic distributions (bottom) at 4-bolt configuration and (a) 8, (b) 12 and (c) 16 N m clamping torques for each pair of bolt and nut in the case of a single cell.

current densities as the clamping torque becomes larger for all 3-bolt configurations. Also shown in Fig. 5(d) is the polarization and power density curves of the single cell at 2-, 4- and 6-bolt configurations and $\tau = 16$ N m. At this clamping torque, the maximum power density increases and the mass transport limitation shifts to higher current densities as the bolt number increases. It is clearly observed that 6-bolt configuration offers the best performance in our experiment. The *V–I* characteristics of the single cell are consistent with the contact pressure measurements shown in Figs. 3 and 4.

As known, the effects of the assembly pressure and the bolt configuration (number of bolts and their positions) on the performance of a PEMFC are mainly attributed to the changes of the interfacial electrical resistance and GDL porosity. The later is directly related to the transport resistance of the gas and liquid water and the mass transport current density. The empirical Eqs. (1)–(4) proposed by Jiang and Chu [8] and Kim et al. [19] were adopted to determine the ohmic resistance and the mass transport limit current density of the cell in a systematic way:

$$E = E_0 - b\ \log(i) - iR - i_m m \exp(n i_m) \quad (1)$$

$$i_m = i - i_d \quad (\text{when } i > i_d) \quad (2)$$

$$i_m = 0 \quad (\text{when } i \le i_d) \quad (3)$$

where, E and i are the cell voltage and current density under load from experimental *V–I* characteristics of a single cell, respectively, E_0 is the estimated open circuit voltage (OCV) reversible potential, b is the Tafel slope and R is the ohmic resistance of the cell. Here, i_m (A), m (Ω) and n (A^{-1}) terms are mass transfer parameters at high current range. The parameters (E_0, b, R, i_m, m, and n) can be obtained by fitting the measured polarization curve with computer simulation. The i_d value in Eq. (2) can be obtained from the calculated curve with Eq. (1). At low current density the electrochemical process is mainly controlled by the activation of the electrodes, while at high current density the electrochemical process is mainly controlled by ohmic and/or mass transfer polarization. Physically, the

Table 1
The statistic pressure values and calculated performance parameters of the single cell at different bolt configurations and clamping torques.

Bolt configuration	2			4			6		
τ (N m)	8	12	16	8	12	16	8	12	16
$\bar{P}$ (MPa)	0.29	0.39	0.43	0.41	0.48	0.51	0.50	0.55	0.56
P′ (MPa)	0.09	0.11	0.11	0.12	0.09	0.09	0.09	0.04	0.03
$P'/\bar{P}$	0.33	0.27	0.26	0.30	0.20	0.18	0.18	0.08	0.06
E_0 (V)	0.86	0.87	0.87	0.89	0.87	0.90	0.91	0.89	0.90
b (mV/decade)	94.6	93.8	92.5	85.9	86.3	83.5	80.7	85.9	83.0
R (Ω cm^2)	0.85	0.83	0.61	0.78	0.59	0.52	0.64	0.49	0.45
W_{max} (W)	8.5	8.7	10.2	10.2	11.8	13.0	12.8	13.3	14.4
i_d (mA cm^{-2})	398	440	460	423	502	560	541	550	571
Experimental OCV	0.90	0.91	0.91	0.91	0.92	0.92	0.92	0.92	0.92

Tafel slope b and ohmic resistance R represent the voltage losses due to activation polarization of both electrodes and ohmic polarization, respectively. i_d is the minimum value of current that causes the voltage deviation from the linearity at the higher current range (mass transport limit current density) and is an objective indicator of the mass transfer limit.

The two main interested parameters, R and i_d are summarized in Table 1 at different combinations of bolt configuration and applied torque, along with parameters E_0 and b. While performing the non-linear regression analysis to determine the values of E_0, b, R, i_m, m and n, the correlation coefficients (R^2 value of the fit) were in the range of 0.990–0.998 to ensure that the fitted model parameters represent the experimental data well. Also shown in Table 1 is the experimental OCV for each case. The experimental OCV nearly keeps constant, with the maximum difference of 0.01 V among all cases. The term E_0 is in the range of 0.86–0.91 V, which is approximately equal to the OCV of the cell. The maximum deviation of the estimated E_0 from the experimental OCV is about 5%. The Tafel slope b of each combination fluctuates in the range of 80.7–94.6 mV per decade and falls in the range of 57–110 mV per decade for Pt/C catalyst reported by Chu and Jiang [6]. The values of ohmic resistance R vary from 0.45 to 0.85 $\Omega\,cm^2$, which is higher than the range of values reported by Giddey et al. [18].

As would be expected, the effects of bolt configuration and clamping torque would reflect on the performance of the fuel cell and contact resistance. Their correlations are worth being further investigated. Fig. 6 shows the scatter plots of W_{max}, $P'/\bar{P}$, R and i_d, versus $\bar{P}$, with the data in Table 1. As seen in Fig. 6(a), the maximum power W_{max} increases monotonically with $\bar{P}$ under the current experiment conditions. When performing a linear regression analysis, a high correlation coefficient (R^2 value of the fit) of 0.91 was obtained. This correlation indicates that the larger mean contact pressure tends to yield the higher maximum power, regardless of the combinations of different bolt configurations and clamping torques in the current experiments. Note that the contact behavior between the components inside the PEM single cell is highly non-linear. The mean pressure does not necessarily increase linearly with the bolt numbers and applying torques. Similarly, in Fig. 6(b–d), $P'/\bar{P}$ and R decrease and i_d increases monotonically with the increase of $\bar{P}$. By performing linear regression analyses, high correlation coefficients of 0.86, 0.85 and 0.9 were obtained for the cases of $P'/\bar{P}$, R and i_d versus $\bar{P}$, respectively. $P'/\bar{P}$, R and i_d exhibit nearly linear relations with $\bar{P}$. These correlations imply that the larger the mean contact pressure, the smaller the contact pressure fluctuation and ohmic resistance and the larger the mass transfer limit, considering the experimental errors. On the other hand, E_0 and b did not show such good linear correlations with $\bar{P}$ (also seen in Table 1). Correlation coefficients of 0.55 and 0.65 were obtained with linear regression analyses, respectively. The Tafel slope b seems to decrease with the number of bolts in general for the single cell. But if one examining the relationship between b and the average contact pressure $\bar{P}$ carefully, b does not decrease with $\bar{P}$ for the single cell. As known, at low current density, the major factors affecting the values of E_0 and b are properties of the electrocatalyst, the cell temperature and the humidification conditions [18]. The present statistic analyses are in consistent with the previous findings. Under the current experiment conditions, the large mean contact pressure ($\bar{P}$) increases the uniformity of contact pressure distribution ($P'/\bar{P}$) and reduces the cell ohmic resistance, especially the contact resistance, without damaging PEM and bipolar plates. This reduction in the contact ohmic resistance consequently increases the maximum power and mass transport limit.

It is well known that both the contact resistance and the through-plane resistance of the GDL decrease with the increase in the clamping pressure until a certain point. However, according to the experimental study of Chang et al. [20] on the effects of the clamping pressure on the performance of a PEM fuel cell, the through-plane resistance is quite small as compared to the

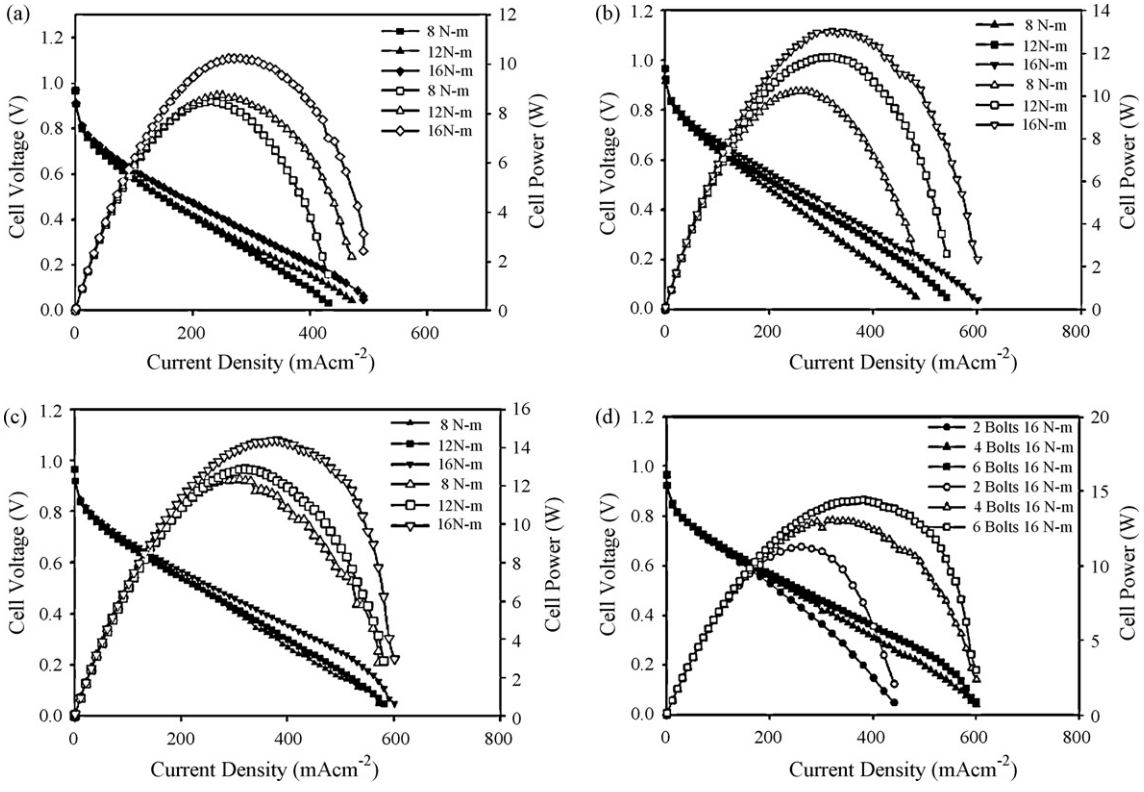

Fig. 5. Polarization and power density curves of the single cell at (a) 2-, (b) 4- and (c) 6-bolt configurations and various clamping torques, and (d) 16 N m clamping torque and different bolt configurations.

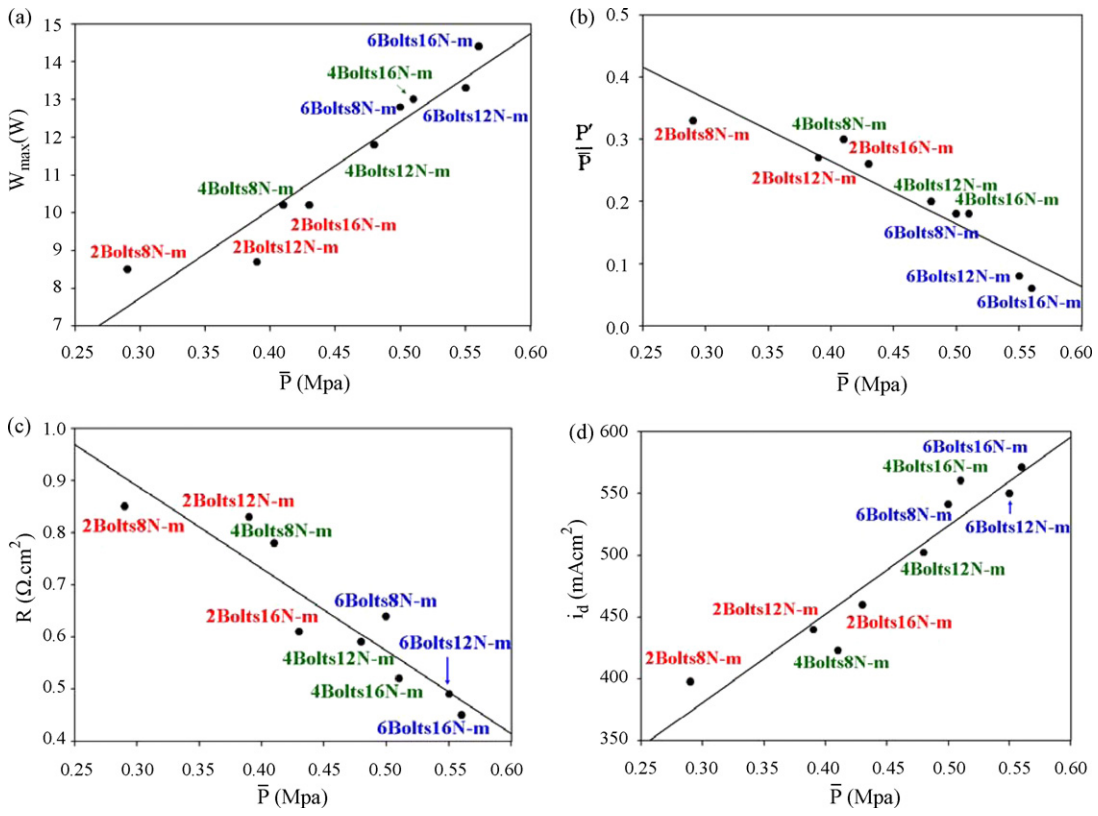

Fig. 6. Scatter plots of (a) W_{max}, (b) $P'/\bar{P}$, (c) R, (d) i_d versus $\bar{P}$ for the single cell.

contact electrical resistance. In the current contact pressure range (<10 bar), the through-plane resistance is less than 4% of the contact resistance (see Fig. 6 in Chang et al. [20]). Therefore, we did not measure or try to isolate the relative contribution of the decrease of the through-plane resistance to the overall increase in the cell performance.

The electro-physical properties of the GDL such as porosity, gas permeability, electrical resistance and thickness were also measured by Chang et al. [20], using a special designed test rig under various clamping pressure levels. In addition to the measurement of the contact resistance between the GDL and the bipolar (graphite) plate under various clamping pressures, their experimental results showed that at the low clamping pressure levels (e.g. <10 bar) increasing the clamping pressure reduces the interfacial resistance between the bipolar plate and the GDL that enhances the electrochemical performance of a PEM fuel cell. In contrast, at the high clamping pressure levels (e.g. >10 bar), increasing the clamping pressure not only reduces the above ohmic resistance but also narrows down the diffusion path for mass transfer from gas channels to the catalyst layers. Comprising the above two effects did not promote the power density too much but reduce the mass-transfer limitation for high current density. Our experimental results are in accordance with that of Chang et al. [20]. Although increasing the mean contact pressure decreases the porosity of the GDL, it does not seem to cause any significant effect on the mass transport in the present experimental range ($\bar{P} < 6$ bar).

3.2. Results of fuel cell stack

Similar statistic analyses of the scanned bitmap images of the pressure-sensitive films were conducted for each cell in the 10-cell stack to obtain its mean value and the standard deviation of the pressure distribution at different combinations of bolt configuration and applied torque. Fig. 7 illustrates a typical example of the measured mean contact pressure $\bar{P}$ and the non-dimensional pressure fluctuation intensity $P'/\bar{P}$ of each cell in the 10-cell stack. The stack was assembled at four bolts and 8 N m. Clear cell-to-cell variations are observed for both $\bar{P}$ and $P'/\bar{P}$. The mean values of cell $\bar{P}$, P' and $P'/\bar{P}$ of the 10 cells at different combinations of bolt configuration and applied torque were calculated and listed in Table 2. Similar to the case of a single cell, $\bar{\bar{P}}_j (\equiv (\sum \bar{P}_j)/M)$ increases with the clamping torque τ at a given bolt configuration, and increases with the bolt numbers at a fixed τ, where M (=10 in the present experiments) is the total number of cells. And, the mean non-dimensional pressure fluctuation intensity of 10 cells $\overline{(P'/\bar{P})_j}$ $(\equiv (\sum (P'/\bar{P})_j)/M)$ again demonstrates an opposite trend to that of $\bar{\bar{P}}_j$ much more evidently than $\overline{P'_j}$. In general, $\overline{(P'/\bar{P})_j}$ decreases with the increase of the clamping torque τ at a given bolt configuration, and decreases with

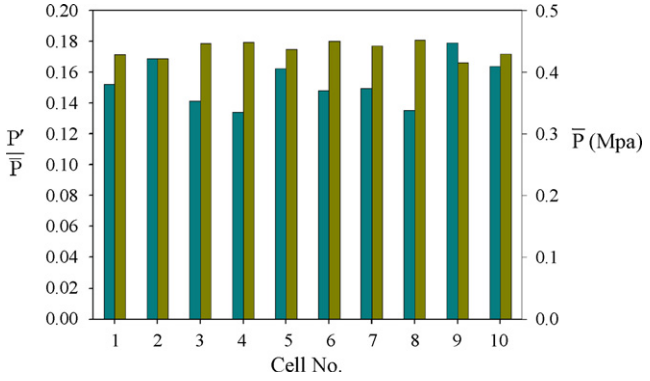

Fig. 7. Typical measured mean contact pressure $\bar{P}$ (right column) and the non-dimensional pressure fluctuation intensity $P'/\bar{P}$ (left column) of each cell in the 10-cell stack. The stack was assembled at four bolts and 8 N m.

Table 2
The statistic pressure values and calculated performance parameters of the 10-cell stack at different bolt configurations and clamping torques.

Bolt configuration	2			4			6		
τ (N m)	8	12	16	8	12	16	8	12	16
$\bar{\bar{P}}_j$ (MPa)	0.36	0.41	0.44	0.43	0.44	0.45	0.46	0.47	0.49
$\overline{P_j}$(MPa)	0.08	0.07	0.07	0.07	0.05	0.05	0.05	0.05	0.02
$\overline{(P'/\bar{P})_j}$	0.21	0.17	0.16	0.15	0.11	0.10	0.11	0.11	0.05
$\sum(E_0)_j$ (V)	10.66	10.52	10.45	10.54	10.52	10.44	10.50	10.50	10.47
$\sum(b)_j$ (mV/decade)	350	393	414	387	393	418	399	400	409
$\sum(R)_j$ (Ω cm^2)	5.5	4.38	3.87	4.49	4.12	3.69	4.41	3.89	3.58
W_{max} (W)	181.7	190.6	205.7	182.5	192.4	208.2	190.7	196.3	214.9
i_d (mA cm^{-2})	330	353	395	311	355	395	361	361	434
Experimental OCV	10.20	10.03	10.01	10.20	10.10	10.20	10.10	10.33	10.10

the increase of the bolt numbers at a fixed τ. Note that $\bar{P'}_j/\bar{\bar{P}}_j$ behaves similarly to $\overline{(P'/\bar{P})_j}$. Comparing Table 1 with Table 2, the $\overline{(P'/\bar{P})_j}$ of the stack is smaller than the corresponding $P'/\bar{P}$ of the single cell at the same combination of bolt configuration and applied torque, indicating less effects of deformation and bending of the end plates on the uniformity of the stack than that of a single cell.

The polarization and power density curves describing the performances of the 10-cell stack at 2-, 4- and 6-bolt configurations are presented in Fig. 8(a–c), respectively. As in the case of the single cell, the maximum power density increases and the mass transport limitation shifts to higher current densities as the clamping torque becomes larger for all 3-bolt configurations. Also shown in Fig. 8(d) is the polarization and power density curves of the 10-cell stack at 2-, 4- and 6-bolt configurations and τ = 16 N m. At this clamping torque, the maximum power density increases and the mass transport limitation shifts to higher current densities as the bolt number increases. Again, it is clearly demonstrated that the combination of 6-bolt configuration and 16 N m clamping torque offers the best performance in our experiment. The *V–I* characteristics of the stack are consistent with the descriptions about the mean contact pressure measurements ($\bar{\bar{P}}_j$) in the previous paragraph.

Eq. (1) was adapted to describe the *V–I* characteristics and estimate the electric resistances and mass transport limiting currents for a PEMFC stack, following the work of Chu and Jiang [6]. Since the current flowing to each cell is the same, the total voltage of the stack is then expressed as follows:

$$\sum(E)_j = \sum(E_0)_j - (\log(i))\sum(b)_j - i\sum(R)_j - i_m m\ \exp(ni_m) \quad (4)$$

Here, the subscript *j* represents the order of a single cell in the stack and $\sum$ takes the sum of all single cells. The two main interested parameters, $\sum(R)_j$ and i_d, obtained by fitting the experimental data

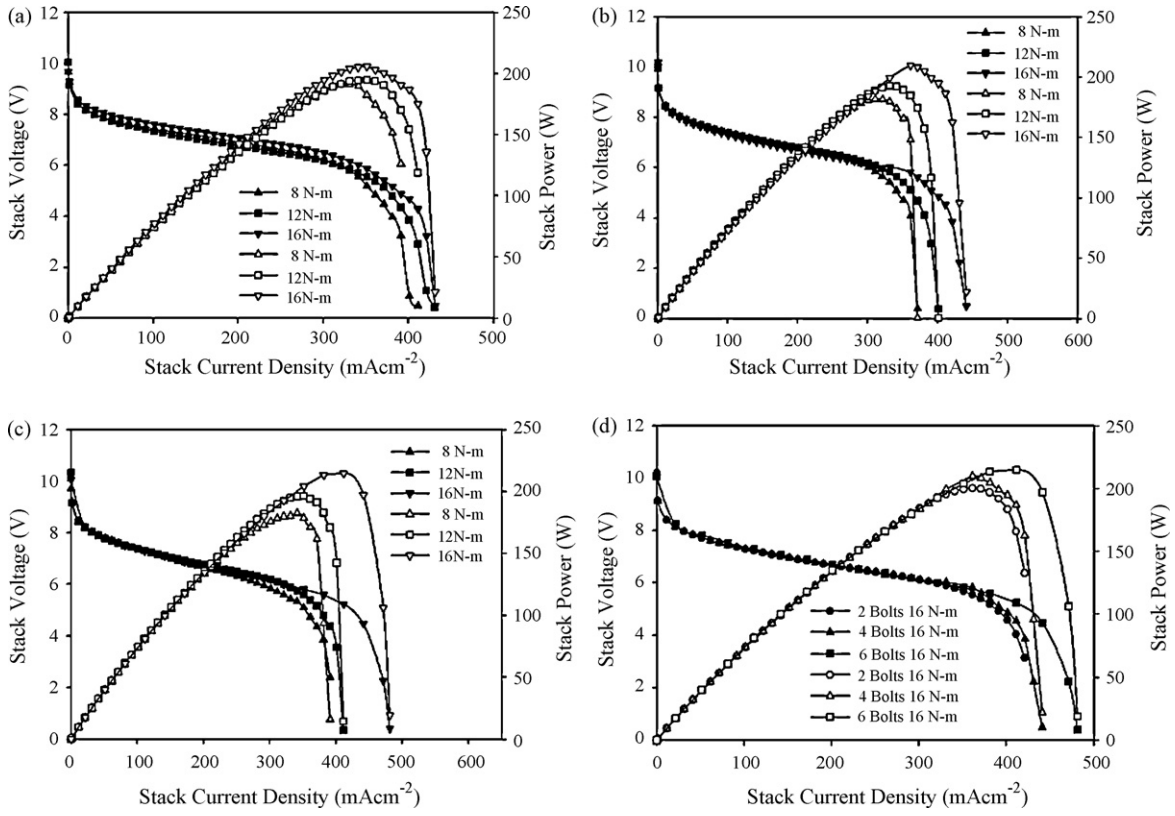

Fig. 8. Polarization and power density curves of the 10-cell stack at (a) 2-, (b) 4- and (c) 6-bolt configurations and various clamping torques, and (d) 16 N m clamping torque and different bolt configurations.

with Eqs. (2)–(4), at different combinations of bolt configuration and applied torque are summarized in Table 2, along with parameters $\sum(E_0)_j$ and $\sum(b)_j$. While performing the non-linear regression analysis to determine the values of $\sum(E_0)_j$, $\sum(b)_j$, $\sum(R)_j$, i_m, m and n, the correlation coefficients (R^2 value of the fit) were in the range of 0.990–0.998. The fitted model parameters represent the experimental data very well. Also shown in Table 2 is the experimental OCV for each case. The experimental OCV nearly keep constant, with the maximum difference of 0.03 V/cell. The maximum deviation of the estimated $\sum(E_0)_j$ from the experimental OCV is about 5%. The term $\sum(E_0)_j$ is approximately equal to the OCV of the stack and is in a small range of 10.44–10.66 V. The values of total ohmic resistance, $\sum(R)_j$ at various combinations of bolt configuration and applied torque vary from 3.58 to 5.5 $\Omega\,cm^2$. The corresponding average ohmic resistance of each cell is in the range of 0.358–0.550 $\Omega\,cm^2$, which is slightly higher than the range of values reported by Giddey et al. [18]. The values of $\sum(b)_j$ vary from 350 to 418 mV per decade. The average values of Tafel slope of each cell fall below the range of 57–110 mV per decade for Pt/C catalyst reported by Chu and Jiang [6], but are in good agreement with the values reported by Kim et al. [19]. As mentioned earlier, at low current density, the major factors affecting the values of $\sum(E_0)_j$ and $\sum(b)_j$ are properties of the electrocatalyst, the cell temperature and the humidification conditions [18]. With the same electrocatalyst, inflow humidification conditions and activation process in all experiments (described in Section 2.3), the average values of E_0 of each cell are higher than that in the corresponding cases of the single cell (Table 1), while the average values of Tafel slope are lower. Generally, $\sum(E_0)_j$ increases with increasing temperature while $\sum(b)_j$ goes in opposite direction [21]. The higher temperature of the stack than that of the single cell yields the differences. The average values of ohmic resistance of each cell are smaller than that in the corresponding cases of the single cell (Table 1), especially for the cases of 2- and 4-bolt configurations. Two possible mechanisms need to be further studied in the future to clarify this reduction in the average ohmic resistance: (1) the improved uniformity of the contact pressure distribution reduces the average contact ohmic resistance and (2) the increased stack temperature promotes the hydration of the membranes under the current experimental conditions and yields the higher ionic conductivity of the Nafion membrane electrolyte and the lower ohmic resistance.

The effects of bolt configuration and clamping torque on the parameters, W_{max}, $\overline{(P'/\bar{P})_j}$, $\sum(R)_j$ and i_d, versus $\bar{\bar{P}}_j$ are further examined by the scatter plots in Fig. 9, with the data in Table 2. Much more scattered features than that of the single cell are observed. As shown in Fig. 9(a), the maximum power W_{max} does not increase monotonically with $\bar{\bar{P}}_j$. When performing a linear regression analysis, a low correlation coefficient (R^2 value of the fit) of 0.49 was obtained. Similarly, in Fig. 9(b–d), $\overline{(P'/\bar{P})_j}$ and $\sum(R)_j$ seem to decrease and i_d to increase with the increase of $\bar{\bar{P}}_j$, but the trends are far from monotonic. By performing linear regression analyses, correlation coefficients of 0.85, 0.77 and 0.43 were obtained for the cases of $\overline{(P'/\bar{P})_j}$, $\sum(R)_j$ and i_d versus $\bar{\bar{P}}_j$, respectively. Only $\overline{(P'/\bar{P})_j}$ and $\sum(R)_j$ show higher linear correlations with $\bar{\bar{P}}_j$, indicating increasing the mean contact pressure improves the uniformity of the contact pressure distribution and reduces the contact ohmic resistance, in general. However, the linear correlation between the mean contact pressure ($\bar{\bar{P}}_j$) and the maximum power (W_{max}) or the mass transport limit (i_d) are not conclusive. $\sum(E_0)_j$ and $\sum(b)_j$ did not show good linear correlations with $\bar{\bar{P}}_j$ either (also seen in Table 2). Correlation coefficients of 0.65 and 0.55 were obtained with linear regression analyses, respectively. For the 10-cell stack, the Tafel slope $\sum(b)_j$ seems to increase with clamping "torque" (not $\bar{\bar{P}}_j$), at the same bolt configuration. For all cases, $\sum(b)_j$ falls in the range

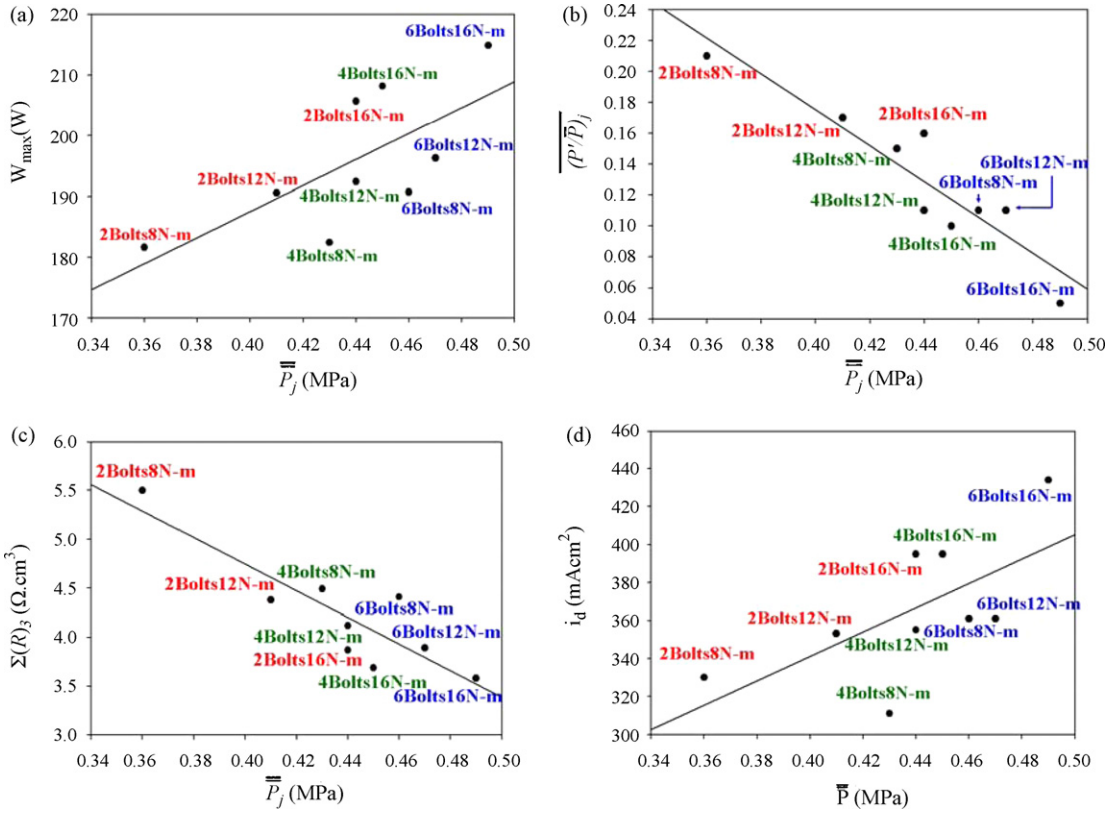

Fig. 9. Scatter plots of (a) W_{max}, (b) $\overline{(P'/\bar{P})_j}$, (c) $\sum(R)_j$, (d) i_d versus $\bar{\bar{P}}_j$ for the 10-cell stack.

of 393–418 (relatively constant), with only one exception at two bolts and 8 N m. Again, $\sum(b)_j$ does not increase with average contact pressure $\overline{\overline{P_j}}$ for the 10-cell stack, by examining carefully the relationship between $\sum(b)_j$ and average contact pressure $\overline{\overline{P_j}}$. The effects of various combinations of bolt configuration and clamping torque on the performance of the stack and the relevant electrode kinetic parameters could not be reflected by a single statistic parameter, mean contact pressure $\overline{\overline{P_j}}$, only. The detailed contact pressure distribution may have important influences on the local electrochemical reactions and heat and mass transfer processes involved in the stack. These local effects are more complicated and important in the stack than that in a single cell. Although, increasing $\overline{\overline{P_j}}$ reduces the contact ohmic resistance generally, a comprehensive study of the influence of the contact pressure distribution on local electrochemical reactions and heat and mass transfer processes is needed to well present the performance of the stack.

4. Conclusion

In this study, systematic statistic analyses were performed to study the effects of different combinations of bolt configuration and clamping torque on the performance and relevant electrode kinetic parameters of a single PEMFC and a 10-cell stack. The mean value and the standard deviation of the pressure distribution of every combination of bolt configuration and applied torque, extracted from the pressure-sensitive films, were calculated. A non-dimensional pressure fluctuation intensity, which indicates the relative dispersion to its mean value, was then proposed to present the uniformity of the contact pressure distribution, similar to the definition of the turbulence intensity in fluid mechanics. From the experimental results of polarization curves and contact pressure measurements, it showed that, for either the single cell or the stack at the same bolt configuration, the maximum power density increases and the mass transport limitation shifts to higher current densities as the clamping torque becomes larger; and that the maximum power density increases as the bolt number increases, when at the same clamping torque. The combination of 6-bolt configuration and 16 N m clamping torque offered the best performances for both the single cell and the stack in our experiments. Moreover, for the single cell under the current experiment conditions, the larger mean contact pressure tends to yield the higher maximum power, regardless of the bolt configuration and the applied torque. The uniformity of the contact pressure distribution, the ohmic resistance and the mass transport limit current had highly linear correlations with the mean contact pressure. Under the current experiment conditions, the large mean contact pressure increases the uniformity of contact pressure distribution and reduces the cell ohmic resistance, especially the contact resistance, without damaging PEM and bipolar plates. This reduction in the contact ohmic resistance consequently increases the maximum power and mass transport limit. Although increasing the mean contact pressure decreases the porosity of the GDL, it does not seem to cause any significant effect on the mass transport in the present experiments. In the case of the 10-cell stack, clear cell-to-cell variations were observed for both cell mean contact pressure and pressure fluctuation intensity. The effects of various combinations of bolt configuration and clamping torque on the stack performance and mass transport limit current could not be reflected by the stack mean contact pressure only. Generally, increasing the mean contact pressure improved the uniformity of the contact pressure distribution and reduced the contact ohmic resistance. However, the maximum power did not increase monotonically with the mean contact pressure. Besides the effect that the improved uniformity of the contact pressure distribution reduces the average contact ohmic resistance, the detailed contact pressure distribution may have important influences on the local electrochemical reactions and heat and mass transfer processes involved in the stack. Overall, there are no conclusive trends for the estimated OCV and Tafel slope with the applied mean contact pressure in either the single cell or the 10-cell stack case. Further studies will be conducted to clarify the role of contact pressure distribution in the stack performance in the future.

Acknowledgment

The present study was supported by the National Science Council, Taiwan, the Republic of China through the grant numbers NSC 96-2221-E-006-157.

References

[1] J. Larminie, A. Dicks, Fuel Cell Systems Explained, Second ed., Wiley, Chichester, 2003, pp. 45–59.
[2] C.M. Carlstrom, Jr., End Plate Assembly Having a Two-Phase Fluid-Filled Bladder and Method for Compressing a Fuel Cell Stack, 2001, US Patent No. 6,200,698 B1.
[3] W.K. Lee, C.H. Ho, J.W. Van Zee, M. Murthy, J. Power Sources 84 (1999) 45–51.
[4] V. Mishra, F. Yang, R. Pitchumani, J. Power Sources 141 (2005) 47–64.
[5] X.T. Wang, Y. Song, B. Zhang, J. Power Sources 179 (2008) 305–309.
[6] D. Chu, R. Jiang, J. Power Sources 83 (1999) 128–133.
[7] S. Giddy, F.T. Ciacchi, S.P.S. Badwal, J. Power Sources 125 (2004) 155–165.
[8] R. Jiang, D. Chu, J. Power Sources 93 (2001) 25–31.
[9] S.J. Lee, C.D. Hsu, C.H. Huang, J. Power Sources 145 (2005) 353–361.
[10] P. Zhou, C.W. Wu, G.J. Ma, J. Power Sources 159 (2006) 1115–1122.
[11] D. Liu, X. Lai, J. Ni, L. Peng, S. Lan, Z. Lin, J. Power Sources 172 (2007) 760–767.
[12] http://www.fujifilm.com/, September 2007.
[13] C.Y. Wen, H.T. Chang, in: J.J. Huang (Ed.), Proceedings of the 3rd National Conference on Hydrogen Energy and Fuel Cell, Tainan, Taiwan, 11–14 November, 2008, Paper no. FC050.
[14] Y. Tang, A.M. Karlsson, M.H. Santare, M. Gilbert, S. Cleghorn, W.B. Johnson, J. Mater. Sci. Eng. A 425 (2006) 297–304.
[15] US Fuel Cell Council, Single Cell Test Protocol, 2006.
[16] Y.S. Lin, Master Thesis, Department of Aeronautics and Astronautics, Cheng-Kung University, Taiwan, 2008.
[17] C.Y. Wen, G.W. Huang, J. Power Sources 178 (2008) 132–140.
[18] S. Giddey, F.T. Ciacchi, S.P.S. Badwal, J. Power Sources 125 (2004) 155–165.
[19] J. Kim, S. Lee, S. Srinvasan, J. Electrochem. Soc. 142 (1995) 2670–2679.
[20] W.R. Chang, J.J. Hwang, F.B. Weng, S.H. Chan, J. Power Sources 166 (2007) 149–154.
[21] C.Y. Wen, Y.S. Lin, C.H. Lu, J. Power Sources 189 (2009) 1100–1105.